INFRARED SPACE OBSERVATORIES: HOW TO MITIGATE ZODIACAL DUST INTERFERENCE

P. GURFIL,[1] J. KASDIN,[1] R. ARRELL,[1] S. SEAGER,[2] AND S. M. NISSANKE[3]

ABSTRACT

Out-of-the-ecliptic trajectories that are beneficial to space observatories such as the *Terrestrial Planet Finder* and other potential mid-IR missions are introduced. These novel trajectories result in a significantly reduced background noise from the zodiacal dust radiation, compared to a 1 AU in-plane orbit. Three types of trajectories are characterized using genetic algorithms. Based on the characterization process, two optimal highly inclined non-Keplerian trajectories that are energetically feasible are derived. The energy requirements to reach these trajectories are respectively half as much and equivalent to a direct trip to 5 AU with no planetary gravitational assists. We use the zodiacal dust model from the *COBE* data to determine how well the optimal trajectories mitigate the interference from the zodiacal dust. The first optimal trajectory can use existing launch technology and yields a maximum decrease of 67% in the zodiacal cloud brightness. The zodiacal brightness for this trajectory is reduced by at least 50% for 60% of the mission lifetime. The second optimal trajectory requires planned improvement in launch technology, but it renders a dramatic 97% maximum noise decrease. The zodiacal cloud brightness is reduced by at least 70% for 82% of the mission lifetime for this trajectory.

Subject headings: infrared: general — space vehicles — space vehicles: instruments

1. INTRODUCTION

An unprecedented interest in space-borne observation missions has arisen out of NASA's Origins Program, a collection of missions aimed at determining and characterizing the origin and development of galaxies, stars, planets, and the chemical conditions necessary to support extraterrestrial life.[4] Over the course of the next 2 decades, the Origins Program will focus on developing space-based observatories through a series of precursor missions such as the *Space Infrared Telescope Facility* (*SIRTF*); first-generation missions such as *Space Technology 3* (*ST3*), the *Space Interferometry Mission* (*SIM*), and the *Next Generation Space Telescope* (*NGST*); and second-generation missions such as the *Terrestrial Planet Finder* (*TPF*).

One of the most important constraints of such missions is the so-called zodiacal dust (zodi) or interplanetary dust. In our own solar system, dust (very tiny solid particles composed of silicates, ices, and other minerals) is ever present. This material is both a remnant of the formation of the planets and a consequence of continuing collisions among comets, asteroids, and other small bodies. The zodi has a potentially serious impact on the ability of space-borne observatories to detect and study their targets. Specifically, the zodi reveals itself as a diffuse component of the sky brightness, attributed to the scattering of sunlight in the UV, optical, and near-IR, and the thermal reradiation of absorbed energy in the mid-IR and far-IR. At infrared wavelengths from approximately 1 μm, the signal from the zodi is a major contributor to the diffuse sky brightness and dominates the mid-IR (10–60 μm) sky in nearly all directions (except for very low Galactic latitudes). Consequently, the emission from the local zodi is a major noise source, considerably affecting the size and weight requirements of

the mirrors of space-borne observatories. Beichman, Woolf, & Lindensmith (1999) show that for a 1 AU *TPF* mid-IR interferometer mission, the local zodiacal background constitutes roughly 70% of the total noise. The intensity of the zodi radiation (in terms of thermal emission) is greatly reduced when moving in a direction normal to the ecliptic plane.

The zodi problem is the principal motivation for the design of trajectories having considerable displacements normal to the ecliptic. We have examined a widely used zodi model that was measured by the *Cosmic Background Explorer* (*COBE*) and the *Infrared Astronomical Satellite* (*IRAS*; Kelsall et al. 1998). Simulation of this model quantifies the evolution of the zodi brightness (from thermal emission only) as a function of the height above the ecliptic plane, at various Earth positions. The results are depicted in Figure 1, with λ denoting Earth's angular position relative to the Sun. It is apparent that at 0.18 AU above the ecliptic plane, more than 50% of the emission is avoided, and at 0.4 AU above the ecliptic, more than 80% of the emission is avoided. While higher excursions further reduce the noise generated by the zodi emission, the energetic requirements involved may be substantial. In other words, the 0.4 AU point on the abscissa of Figure 1 represents a threshold above which the dependence of the normalized brightness on the height above the ecliptic plane is small when compared to the energy cost to get there.

A variety of orbits have been considered for other missions. The diversity of these missions and their stringent resolution and accuracy requirements necessitate the design of specialized trajectories. For example, for the *NGST* mission, a halo orbit around the colinear Lagrangian libration point has been considered.[5] For the *TPF* and *Darwin* missions, orbits at 5 AU where the zodi is highly reduced are being considered (Landgraf & Jehn 2001), but cost, communication, power, and delay to data return can be problematic. For the *TPF* mission, both L_2 and heliocentric Earth-trailing orbits have also been examined (Beichman et al. 1999). To date, several types of trajectories

[1] Department of Mechanical and Aerospace Engineering, Princeton University, Princeton, NJ 08544.

[2] Institute for Advanced Study, Einstein Drive, Princeton, NJ 08540.

[3] Department of Physics, Cavendish Laboratory, Madingley Road, Cambridge University, Cambridge CB3 0HE, UK.

[4] Available at http://origins.jpl.nasa.gov.

[5] Available at http://icarus.stsci.edu/~lubow/ngst/orbits.html.
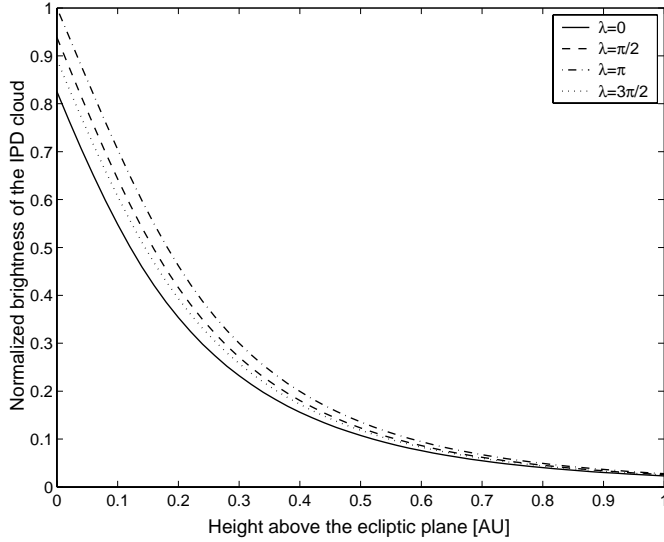
Fig. 1.—Variation of the brightness of the local interplanetary dust cloud (thermal emission only) as viewed from Earth along the line of sight normal to the ecliptic plane (λ, the heliocentric longitude) at the four different Earth positions indicated in Fig. 2.

associated with the colinear libration points have been reported. These trajectories are obtained by exploring either the planar circular restricted three-body problem (CR3BP) or the spatial CR3BP. The so-called Lyapunov orbits obtained in the planar case (Szebehely 1967) bifurcate into a spatial family of Lissajous orbits (Gomez, Massdemont, & Simo 1997), which generate the well-known Halo orbits as a particular case only when perturbations are ignored and specific initial conditions are selected (Howell, Barden, & Lo 1997; Henon 1974; Goudas 1963). While libration-point orbits have been widely explored (as they often offer valuable operational and scientific features), less attention has been given to other trajectories emerging from the spatial CR3BP that are more suitable for the unique constraints of mid-IR space-borne observation missions.

This paper describes work aimed at synthesizing families of out-of-the-ecliptic trajectories, which mitigate the effects of the zodi. Section 2 discusses the zodi model, § 3 describes the optimal trajectories, and § 4 follows with a summary and discussion.

2. THE LOCAL ZODIACAL CLOUD MODEL

A parameterized physical model of the zodi was used to evaluate the effectiveness of the orbits described in this paper. This model is a simplified version of the highly complex model developed in direct conjunction with the measurements from the *COBE* DIRBE satellite (Kelsall et al. 1998).

As the following equation and discussion demonstrate, the model brightness is calculated as the integral of the product of a source function and a three-dimensional dust density distribution function evaluated along the line of sight:

$$I_\nu = \int E_{c,\nu} B_\nu(T(R)) n_c(X, Y, Z)\, ds . \quad (1)$$

At infrared wavelengths of approximately 10–60 μm, thermal reradiation of absorbed energy from the zodi is estimated to contribute 90% or more to the total sky brightness in nearly all directions (except at very low Galac-

tic latitudes). In contrast, the scattered sunlight contribution is of significance in the UV, optical, and near-IR. Therefore, as a first approximation, it can be neglected in the case of an observing mission centered at a 12 μm wavelength. The simplified model thus considers the thermal emission contribution of the zodi, which is expressed in equation (1) as a blackbody $B_\nu(T(R))$ and its associated emissivity modification factor at 12 μm $E_{c,\nu}$ (initially a free parameter in the original DIRBE model), which is $E_{c,12\,\mu m} = 0.958$. The dust-grain temperature T variation with distance from the Sun is given by $T(r) = T_0 R^{-\delta}$, where $\delta = 0.467$. The three-dimensional dust density distribution $n_c(X, Y, Z)$ is composed of several structured components: a smooth cloud, three asteroidal dust bands, and a circumsolar ring at 1 AU. At a wavelength of 12 μm, the DIRBE instrument (Kelsall et al. 1998) measured the zodi components of the smooth cloud, dust bands, and circumsolar ring as 28.476, 1.938, and 3.324 MJy sr^{-1}, respectively. The simplified model adopted in this paper neglects the contribution to the zodi brightness of the dust bands and circumsolar ring.

Because of the relatively small inclination of the midplane of the smooth cloud distribution, the zodiacal light is the only component of the sky brightness that is not fixed on the celestial sphere. This important and unique feature, depicted in Figure 2, results in the temporal variation of zodi brightness observed in a given celestial direction by an Earth-based observer. The model calculations for a spacecraft are performed in heliocentric ecliptic coordinates (X, Y, Z), where s, $R_\oplus$, and λ represent respectively the height above Earth, the Earth-Sun distance (1 AU), and the heliocentric longitude of Earth:

$$X = R_\oplus \cos \lambda , \quad (2)$$
$$Y = R_\oplus \sin \lambda , \quad (3)$$
$$Z = s . \quad (4)$$

The center of the smooth cloud is offset from the Sun by (X_0, Y_0, Z_0), and the resulting translated cloud coordinates are

$$X' = X - X_0 , \quad (5)$$
$$Y' = Y - Y_0 , \quad (6)$$
$$Z' = Z - Z_0 , \quad (7)$$
$$R_c = \sqrt{X'^2 + Y'^2 + Z'^2} . \quad (8)$$

The vertical structure of the smooth dust cloud is determined by the height of its inclined symmetric midplane,

$$Z_c = X' \sin \Omega \sin i - Y' \cos \Omega \sin i + Z' \cos i , \quad (9)$$

where i and Ω are the inclination and ascending node of the midplane, respectively.

The density of the smooth cloud is separable into radial and vertical terms,

$$n_c(X, Y, Z) = n_0 R_c^{-\alpha} f\left(\left|\frac{Z_c}{R_c}\right|\right), \quad (10)$$

where

$$f\left(\left|\frac{Z_c}{R_c}\right|\right) = \begin{cases} e^{-\beta(|Z_c/R_c|^2/2\mu)^\gamma} & \left|\frac{Z_c}{R_c}\right| < \mu , \\ e^{-\beta(|Z_c/R_c|^2 - \mu/2)^\gamma} & \left|\frac{Z_c}{R_c}\right| \geq \mu . \end{cases} \quad (11)$$
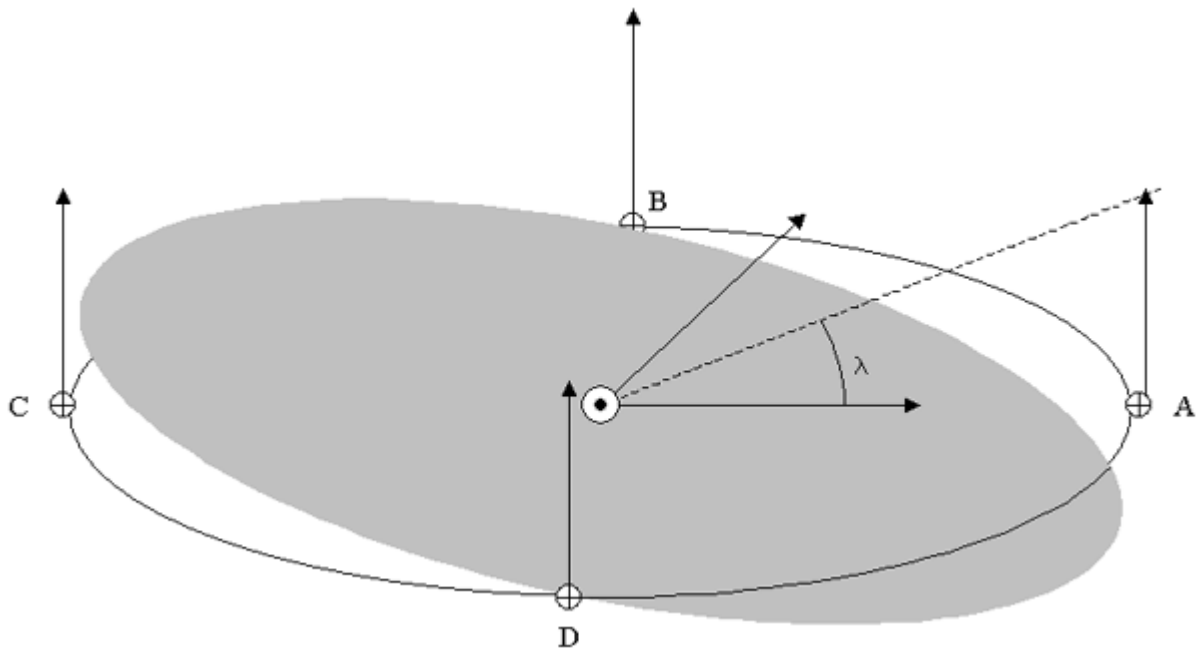
Fig. 2.—Inclination of the symmetric zodi cloud with respect to the Sun-Earth ecliptic plane. A, B, C, and D correspond to the positions of the line of sight ($\lambda = 0$, $\pi/2$, $\pi, 3\pi/2$) shown in Fig. 1.

Following the same procedure as the DIRBE model, integration along the line of sight was performed from the satellite to an outer radial cutoff of 5.2 AU from the Sun. A particular line of sight is defined by two angles, the projected angle in the ecliptic plane and the angle from the ecliptic. To evaluate the zodi at a particular point along the orbit, a single angle from the ecliptic (usually 30°) was used, and the zodi brightness was averaged over 360° of the projected angle; these numbers were then normalized to range from 0 to 1.

3. TRAJECTORIES

3.1. The Equations of Motion

A vast amount of literature exists on the CR3BP (e.g., Gomez, Masdemont, & Simo 1998; Gomez et al. 1997; Howell et al. 1997; Marchal 1990; Szebehely 1967, and references therein). In almost all past research, the standard rotating coordinate system has been used with the origin set at the barycenter of the large primary m_1 and the small primary m_2. The x-axis is positive in the direction of m_2, the z-axis is perpendicular to the plane of rotation and is positive when pointing upward, and the y-axis completes the set to yield a right-hand reference frame. Normalization is performed by setting $m_2 = \mu$ and $m_1 = 1 - \mu$, where $\mu = m_2/(m_1 + m_2)$. Thus, m_1 is located at $(\mu, 0, 0)$ and m_2 is located at $(\mu - 1, 0, 0)$. Usually, this coordinate system is sufficient to model the problem and yields a fruitful characterization of diverse families of trajectories. However, in this study we have adopted a slightly different rotating coordinate system, which we found to be particularly useful for characterization of trajectories that reduce the zodi interference. The basic notion is to choose the origin of the coordinate system at the center of the small primary, Earth in our case, rather than the barycenter, and to normalize the masses by the mass of the large primary, the Sun in our case. This coordinate system was first used by Rabe (1961) and

later by Breakwell (1963) in their approximate analyses of three-dimensional trajectories.

Following the usual analysis, but in this variant coordinate system, let r denote the position vector of the vehicle relative to Earth and R that of Earth relative to the Sun. The acceleration of the spacecraft relative to Earth is given by Breakwell (1963),

$$\ddot{r} = -\frac{\mu_E r}{r^3} - \left[\frac{\mu_S(R + r)}{|R + r|^3} - \frac{\mu_S R}{R^3}\right], \qquad (12)$$

where μ_E is the gravitational constant of Earth and μ_S is the gravitational constant of the Sun.

The acceleration $\ddot{r}$ is evaluated in a rotating Earth-fixed coordinate system as depicted in Figure 3. This local vertical reference frame originates at the center of Earth, with the x-axis directed radially outward along the local vertical, the y-axis lying along the direction of Earth's motion, and the z-axis normal to the ecliptic to complete the Cartesian right-hand setup.

We use the following unit convention: the position of the vehicle is measured in astronomical units (AU), where the mean Earth-Sun distance, assumed constant, is $|R| = R = 1$ AU $= 1.496 \times 10^8$ km. The time unit is normalized by Earth's mean heliocentric angular velocity, i.e., $t = t^*/(R^3/\mu_S)^{1/2}$ with t^* as the time measured in seconds. Accordingly, the velocity vector of the vehicle $v = [\dot{x}, \dot{y}, \dot{z}]^T$ is normalized by $R/(R^3/\mu_S)^{1/2}$. Also, let $\mu = \mu_E/\mu_S$.

The inertial frame used here, denoted by (X, Y, Z), is a heliocentric-ecliptic coordinate system, as depicted in Figure 3. By utilizing the above unit convention, the transformation from the rotating frame to the inertial frame can be found:

$$\begin{bmatrix} X \\ Y \\ Z \end{bmatrix} = \begin{bmatrix} \cos t & -\sin t & 0 \\ \sin t & \cos t & 0 \\ 0 & 0 & 1 \end{bmatrix} \begin{bmatrix} x + 1 \\ y \\ z \end{bmatrix}. \qquad (13)$$
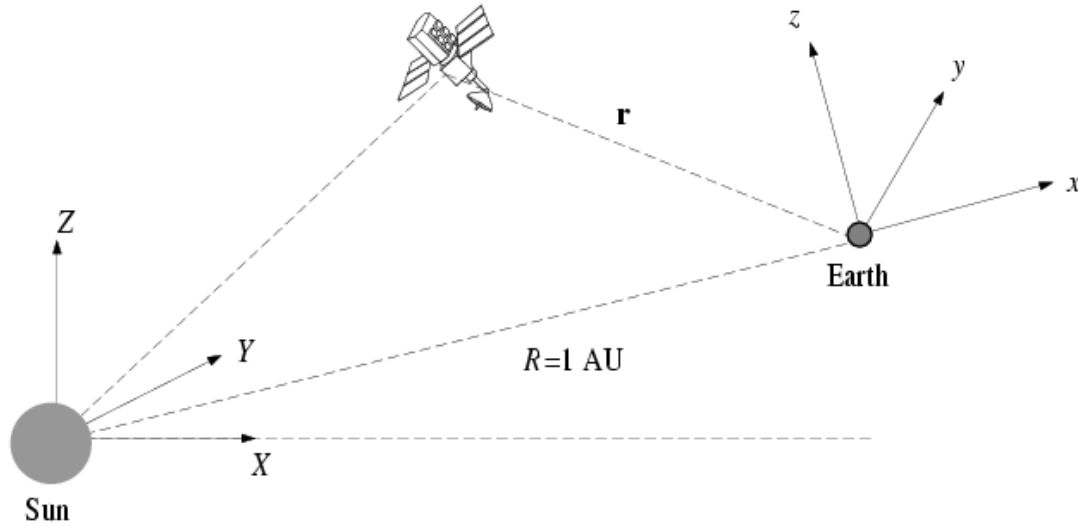
Fig. 3.—Definition of coordinate systems

Also, we define a pseudopotential function

$$\Omega(x, y, z) = \frac{1}{2}(x^2 + y^2) + \frac{\mu}{r} + \frac{1}{\rho} + x , \quad (14)$$

where

$$r = \sqrt{x^2 + y^2 + z^2} \quad (15)$$

is the distance from Earth, and

$$\rho = \sqrt{(x + 1)^2 + y^2 + z^2} \quad (16)$$

is the distance from the Sun.

To proceed, we assume that the vehicle performs a ballistic motion, i.e., no control forces are used, and that the motion of the vehicle is undisturbed by other gravitational sources and the solar radiation pressure. Computing the well-known expression for acceleration in a rotating coordinate frame yields the following equations of motion,

$$\ddot{x} - 2\dot{y} = \Omega_x , \quad (17)$$
$$\ddot{y} + 2\dot{x} = \Omega_y , \quad (18)$$
$$\ddot{z} = \Omega_z , \quad (19)$$

where the subscript stands for partial differentiation. Substituting from equation (14), equations (17)–(19) can be equivalently written as

$$\ddot{x} - x - 2\dot{y} = -\frac{\mu x}{(x^2 + y^2 + z^2)^{3/2}}$$
$$- \frac{(1 + x)}{[(x + 1)^2 + y^2 + z^2]^{3/2}} + 1 , \quad (20)$$

$$\ddot{y} - y + 2\dot{x} = -\frac{\mu y}{(x^2 + y^2 + z^2)^{3/2}}$$
$$- \frac{y}{[(x + 1)^2 + y^2 + z^2]^{3/2}} , \quad (21)$$

$$\ddot{z} = -\frac{\mu z}{(x^2 + y^2 + z^2)^{3/2}}$$
$$- \frac{z}{[(x + 1)^2 + y^2 + z^2]^{3/2}} , \quad (22)$$

or, in state-space vector form,

$$\dot{x} = f(x) , \quad (23)$$

where

$$x \equiv [x, \dot{x}, y, \dot{y}, z, \dot{z}]^T . \quad (24)$$

Multiplying equations (20)–(22) by $\dot{x}$, $\dot{y}$, and $\dot{z}$, respectively, adding the results, and performing the integration renders the integral of motion, the well-known Jacobi constant, given by

$$C = \Omega(x, y, z) - \frac{1}{2}(\dot{x}^2 + \dot{y}^2 + \dot{z}^2) . \quad (25)$$

Note that for any given initial conditions, the differential equations (20)–(22) are equivariant under the following transformations:

$$(x, y, z, t) \rightarrow (x, -y, z, -t) \text{ or } (x, -y, -z, -t) . \quad (26)$$

Hence, symmetries exist only for a backward integration of the equations of motion. However, various symmetries exist for different sets of initial conditions. An obvious symmetry that occurs in the x-z plane is

$$x(t, (x_0)_1) = x(t, (x_0)_2), \quad y(t, (x_0)_1) = y(t, (x_0)_2) ,$$
$$z(t, (x_0)_1) = -z(t, (x_0)_2) , \quad (27)$$

where

$$(x_0)_1 = [x_0, \dot{x}_0, y_0, \dot{y}_0, z_0, \dot{z}_0]^T ,$$
$$(x_0)_2 = [x_0, \dot{x}_0, y_0, \dot{y}_0, -z_0, -\dot{z}_0]^T . \quad (28)$$

Other symmetries that may exist as functions of initial conditions are much less obvious, because of the rotation of the coordinate system. The next section describes some stability considerations that pave the way to synthesizing the constraints for the trajectory optimization procedure.

3.2. Practical Stability

One of the most important aspects of designing a trajectory is to define, study, and characterize its stability. Since stability is a matter of definition, one has to use an appropriate stability framework that is suitable to the specific dynamical system involved. We have found that the so-called practical-stability theory renders a good means for

quantifying our analysis and design of the CR3BP trajectories.

For given initial conditions, a trajectory is said to be practically stable if $r \leq \beta = r_{max}$ for $t \in [t_1, t_2]$, i.e., if the vehicle has not gone beyond some prespecified distance from Earth in a given time interval. This stability definition is used to constrain the genetic algorithm optimization procedure (see § 3.3 below). It reflects operational considerations, since at long distances from Earth, communication becomes too costly.

Regions of practically stable motion for the spatial CR3BP can be semianalytically determined by examining the curves of zero velocity, also known as Hill's regions. These curves are generated by plotting equipotential contours of the function in equation (14), or equivalently, plotting the position of the vehicle for different values of the Jacobi constant evaluated along $\dot{x} = \dot{y} = \dot{z} = 0$. The permissible regions of the vehicle motion are confined by different values of C. For the three-dimensional case discussed here, sufficiency conditions for practically stable motion can be determined as follows (Szebehely 1967): let $C(L_1,0)$ denote the Jacobi constant for the Sun-Earth system evaluated along the zero-velocity curve that intersects the Lagrangian equilibrium point L_1. If

$$C > C(L_1,0) = 1.0004513 , \qquad (29)$$

then the zones of possible motion of the vehicle are divided into three disconnected parts: near Earth, near the Sun, or far away from both. The first two regions are practically stable and are known as Hill-stable regions (Marchal 1990). To distinguish between the practically stable regions and the third (not necessarily practically stable) region, we notice that the vehicle can drift away from the primaries only if the gradient of its potential function is positive. Hence, if equation (29) holds, and in addition

$$\nabla\Omega(x, y, z) < 0 , \qquad (30)$$

a practically stable motion results.

Unfortunately, in order to satisfy both equations (29) and (30), one has to choose impractical initial conditions, since, generally speaking, orbits around Earth have a small normal-motion magnitude and trajectories that start near the Sun, which potentially have large normal deflections, can impose undesirable practical constraints on the mission. Instead, we look for different values of C that also result in practically stable trajectories (recall that the conditions above for stability are sufficient but not necessary). The basic requirement is to find initial conditions that lie within a reasonable distance from Earth, but shift the vehicle to some (possibly) heliocentric orbit inclined to the ecliptic with the least possible energy. This task is fulfilled in the next section.

3.3. Optimal Trajectories

The discussion in the previous section stresses the complexity and counterintuitive nature of solutions to the spatial CR3BP. We used a genetic algorithm (GA), specifically the deterministic crowding GA (S. W. Mahfoud 1995, private communication),[6] to optimize the trajectories. This method is preferable over other optimization algorithms

such as the gradient search and the simplex method because it avoids local minima (i.e., the search is performed over the entire state space) and promotes diversity of solutions. We emphasize that the use of a GA to optimize trajectories in the context of the CR3BP is a new idea, and this paper presents the first implementation of it. Gurfil & Kasdin (2001) give the complete details on the GA optimization mechanism.

We wish to maximize the normal displacement subject to the following:

1. The differential equations of motion.
2. The practical stability constraint: the vehicle should not exceed a given distance from Earth during a given time interval.
3. The initial position vector lying outside Earth's sphere but inside some predetermined radius.
4. The initial velocity vector not exceeding some prespecified limit, derived from the overall propellant mass and capability of the launch vehicle.

See Gurfil & Kasdin (2001) for the GA parameters used for the trajectory optimizations. The trajectory search procedure is divided into two conceptual stages: characterization and design. The purpose of the characterization is to obtain an astrodynamic database of types of trajectories having large out-of-the-ecliptic displacements while using loose search limits (that is, large allowable initial distance from Earth and large launch energy). In the design stage we tighten the optimization constraints (namely, reduced maximum allowable initial distance from Earth and maximum launch energy). The resulting design trajectories can then be categorized based on the trajectory type database obtained from the characterization phase.

3.4. Trajectory Characterization

Eight optimization sets were carried out with different upper and lower bounds on the initial conditions and the maximum permissible distance from Earth (see Gurfil & Kasdin 2001). In order to visualize the trajectories obtained, the trajectory with the highest fitness in the last generation is selected as the optimal solution. The timescale selected for visualization purposes is 15 yr (larger than the 5 yr timescale selected in the optimization itself).

The top-left panel in Figure 4 depicts the three-dimensional trajectory that results from the one of the optimization sets. In this case the GA generates a quasi-periodic Lissajous trajectory that spirals above the ecliptic plane. In other words, if ω_z denotes the frequency of the vertical motion and ω_x and ω_y denote characteristic frequencies of the radial and transverse motions, respectively, then this trajectory satisfies

$$\omega_z < \omega_x \approx \omega_y , \qquad (31)$$

which results in a large fraction of the orbit being above the ecliptic. Trajectories satisfying equation (31) are categorized as type I trajectories. The main deficiency of type I trajectories is their considerable distance from Earth. Note also that the solution depicted in the top-left panel of Figure 4 is asymmetric relative to the ecliptic plane, since most of the time the vehicle remains above the ecliptic. However, due to the symmetry property in equation (27), a mirror image of the trajectory relative to the ecliptic can easily be generated. This is true for all the trajectories considered.

---

[6] See laboratory report 95001 at http://www-illigal.ge.uiuc.edu/index.php3.
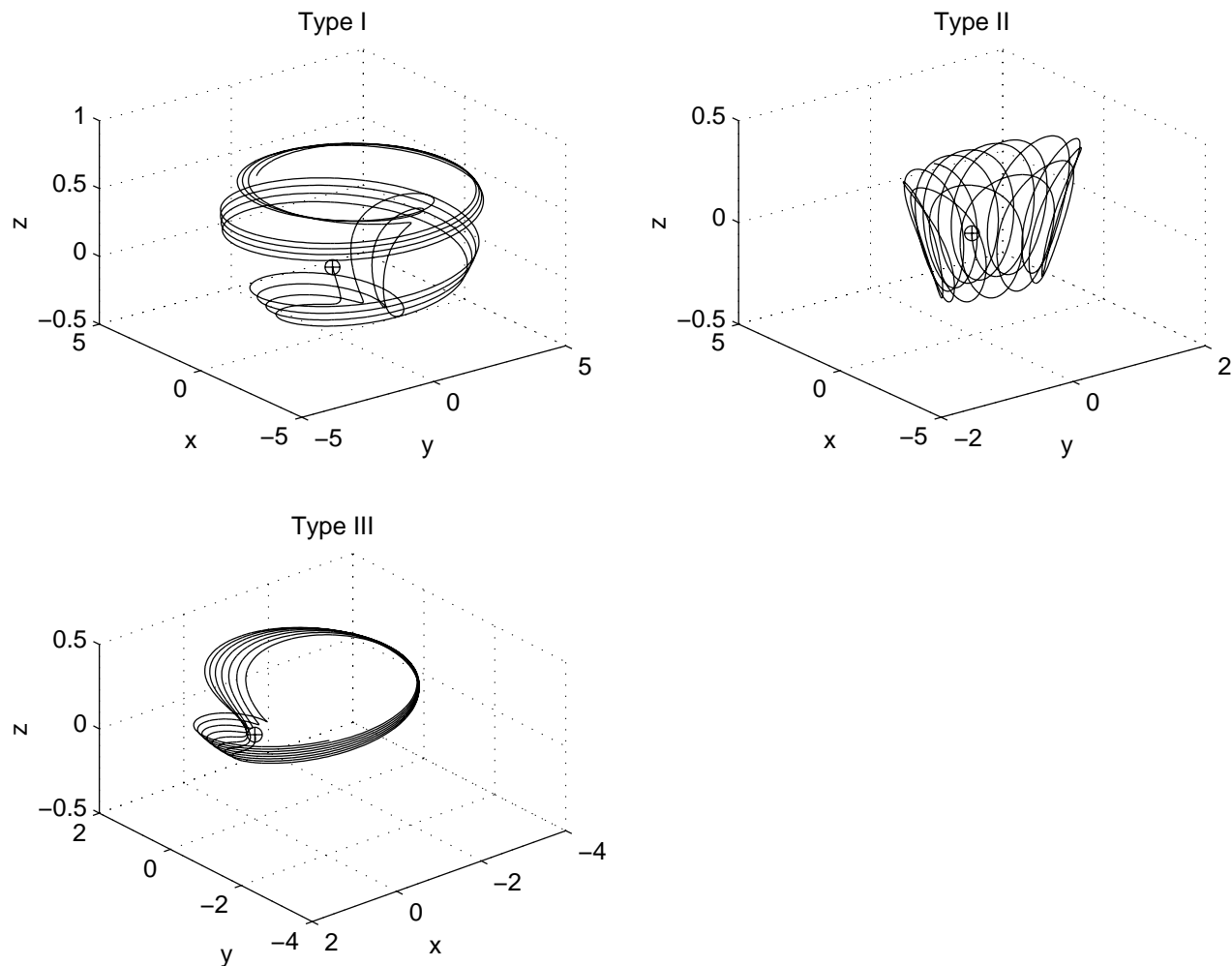
Type I

Type II

Type III

Fig. 4.—Type I, II, and III trajectories resulting from the characterization process shown in an Earth-fixed rotating coordinate system

The top-right panel in Figure 4 depicts the three-dimensional trajectory that results from another optimization set. In this case the GA also generates a quasi-periodic Lissajous trajectory. However, here the trajectory satisfies[7]

$$\omega_z > \omega_x \approx \omega_y , \qquad (32)$$

which results in frequent vertical crossings of the ecliptic while maintaining a reasonable distance from Earth. Trajectories satisfying equation (32) are categorized as type II trajectories. The main deficiency of type II trajectories is that frequent ecliptic crossing reduces the overall duration above a certain height. As with type I, the vertical crossing is asymmetric.

A third type of trajectory, shown in the bottom-left panel of Figure 4, was spotted when performing the characterization on yet a third optimization set. It satisfies the condition

$$\omega_z \approx \omega_x \approx \omega_y . \qquad (33)$$

Thus, the trajectory is actually a quasi-periodic Lissajous trajectory as well, but it is almost closed in three dimensions

because of equation (33), as illustrated by the bottom-left panel of Figure 4.

A further examination shows that the other optimization sets produce type I, II, and III trajectories as well. Generally speaking, reducing the practical stability limit reduces the frequency of the in-plane motion while keeping the frequency of the vertical motion almost unchanged. Reducing the initial velocity limit reduces the amplitude of both the vertical and the in-plane motion. The next step is to narrow the search space in order to design practical operational trajectories for space-borne observation missions. This step is carried out using GAs as well.

3.5. Trajectory Design: Low-Energy Optimal Trajectory

The design procedure is different from the characterization process, as the constraints of the problem are determined based on engineering considerations. We use the database of trajectory types obtained from the characterization process, yet we reoptimize the trajectories based on concrete engineering limitations; the major limitation is the maximum energy available from the launcher for vehicle injection. We used twice the energy per unit mass required to inject a vehicle into an Earth-departure hyperbola starting from a circular orbit of radius r_0 as our design constraint (this measure is known as C3).

[7] In this case, ω_x and ω_y denote the frequencies of the dominant harmonics.

To simplify the discussion, we describe only the first stage of the iterative design procedure. To this end, we choose to start from a 200 km parking orbit, i.e., $(r_0)_{max} = 6578$ km. Next, an estimate of the mass should be made. We choose the benchmark value 4000 kg, which is roughly the estimated mass of the current *TPF* configuration (Beichman et al. 1999). Using charts of lift capabilities versus C3 for various launchers, it was found that the Atlas ARS or the Delta IV could provide a C3 of approximately 40, given this mass. This C3 is smaller than the C3 required for the generation of orbits normal to the ecliptic using planetary flybys (Buglia 1973) or direct injection (Renard 1970). Consequently, assuming C3 $= 40$ km^2 s^{-2} and $(r_0)_{max} = 6578$ km, the maximal allowable initial velocity is $(v_0)_{max} = 12.7$ km s^{-1}. Also, we let $r_{max} = 2$ AU.

Using the constraints mentioned, the GA was used to generate a population of optimal trajectories. The last generation of the GA optimization comprises several solutions, but two dominant solutions stand out (because of the symmetry property). Because the midplane of the zodiacal cloud is inclined 2°.03 to the ecliptic, with the ascending node at 77°.7, going above the ecliptic renders slightly better reduction in zodi noise than going below the ecliptic. Hence, the initial conditions giving a positive normal displacement were chosen.

The optimization procedure will always pick v_0 and C3 to lie on the constraint surface. Thus, properties of the low-energy optimal trajectories are as follows: $v_0 = 12.7$ km s^{-1},

C3 $= 40$ km^2 s^{-2}, and accordingly, $\Delta v = 4.9$ km s^{-1}. The trajectory starts from a 200 km parking orbit. The maximum normal deflection above the ecliptic is 0.223 AU with a maximum distance of 2 AU from Earth. Examining this optimal trajectory in the inertial reference frame from equation (13) reveals that it is non-Keplerian. By non-Keplerian we mean that Earth exerts a gravitational force on the spacecraft that perturbs the motion from the ideal heliocentric case. The repeated Earth encounters cause the trajectory to be diverted a few hundreds of thousands of kilometers away from the Keplerian heliocentric orbit. The distance from the Sun satisfies $0.984 \leq \rho \leq 1.124$, for a mission lifetime of 5 yr. The latter property is most important when considering solar arrays and power management for the mission, since it implies that modest-sized solar arrays can be used. Comparing the frequencies of the in-plane motion with the frequency of the normal motion classifies this trajectory as type II.

Figure 5 depicts the normal, transverse, and radial displacements in the rotating Earth-fixed coordinate system and the distance from Earth for a 5 yr mission for the low-energy optimal trajectory. The three-dimensional trajectory is presented as well. Because of the limited timescale, it seems as though the trajectory drifts away from Earth; however, the transverse and radial displacements are periodic, having very slow frequencies relative to the frequency of the normal motion; hence, a type II trajectory results.
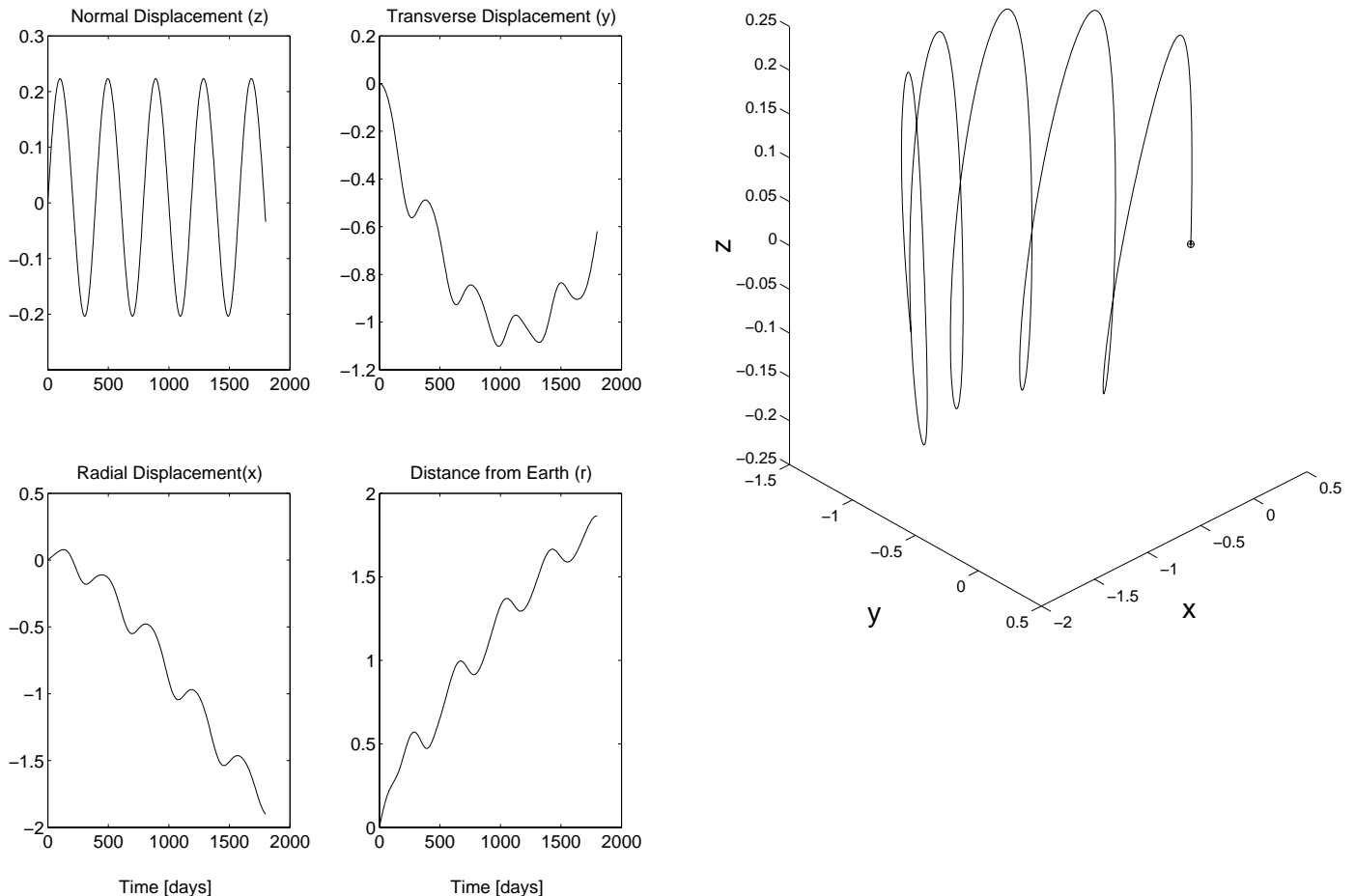

Fig. 5.—Time histories of the displacement components, the three-dimensional trajectory, and the distance from Earth for the low-energy optimal trajectory.

In order to estimate how much the proposed trajectory reduces the zodi noise, we used the zodi model described in § 2 and incorporated it into the integration of the differential equations (20)–(22) using an appropriate coordinate transformation. Figure 6 describes the time history of the normalized zodiacal dust brightness for observation angles of 30°–90° relative to the ecliptic along the low-energy optimal trajectory. First, note the periodic behavior resulting from the periodic normal displacement; in fact, these two variables are coherent. Second, for a positive normal displacement, the reduction in zodi brightness is 5% higher than for negative normal displacement. The maximum reduction in brightness is 67%. Averaging the values over time yields a mean reduction of 45%. Practically speaking, during 60% of the mission lifetime, the zodi brightness is reduced by more than 50%. This allows for a considerable reduction in mirror size, permits faster data integration times, and allows the collection of more observations for a given mission lifetime. Figure 7 shows a plot of the trajectory in heliocentric coordinates, in which the intensity of the plot represents the normalized zodi brightness. Figure 8 is the cumulative brightness distribution for this trajectory. This represents the percentage of the mission lifetime for which the normalized zodi brightness is below a certain value.
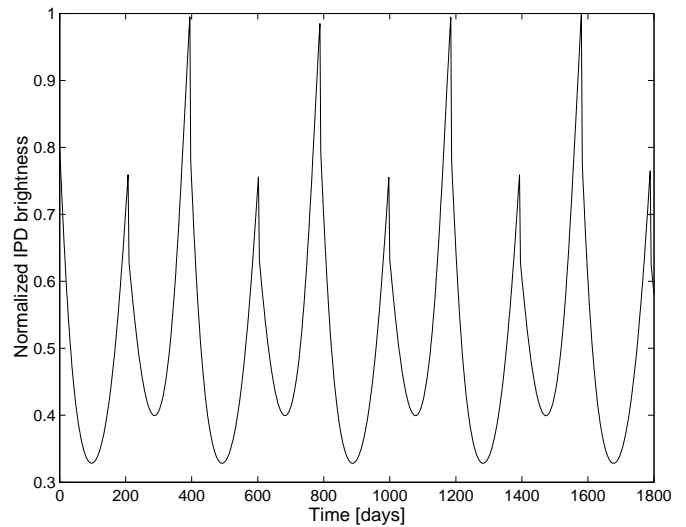

Fig. 6.—Time history of the normalized zodi brightness for observation angles of 30°–90° relative to the ecliptic along the low-energy optimal trajectory. The maximum reduction in brightness is 67%. The spacecraft would observe the sky away from the ecliptic plane; when the spacecraft crossed the ecliptic plane, it would turn over.
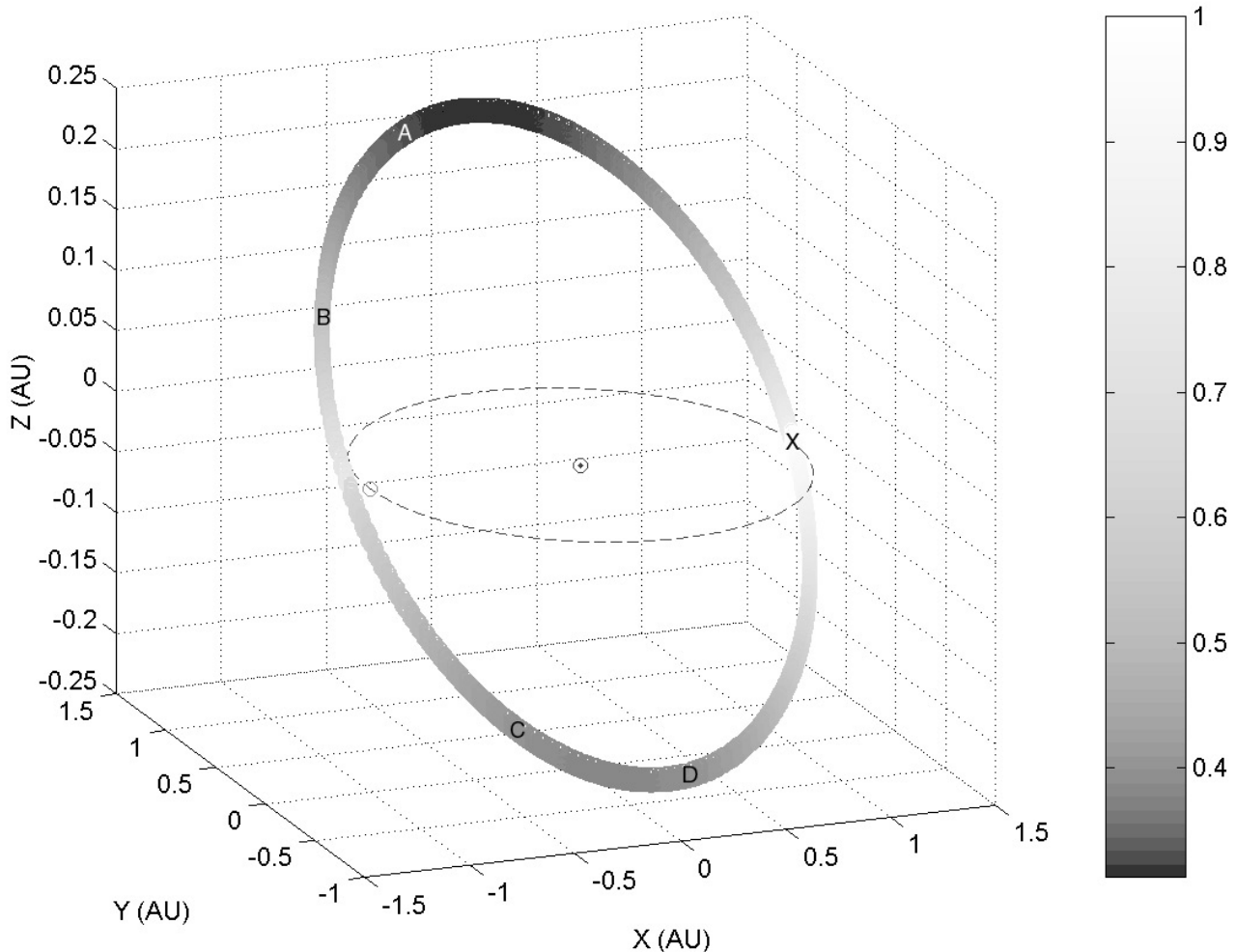

Fig. 7.—Normalized average zodi brightness for the low-energy trajectory, shown in inertial heliocentric-ecliptic coordinates with the position of the Sun indicated by "⊙." A, B, C, and D indicate the position along the trajectory at 6, 12, 18, and 24 months, respectively. The dashed line represents Earth's trajectory, with the position of Earth at 0 and 6 months indicated by the X and O symbols, respectively.
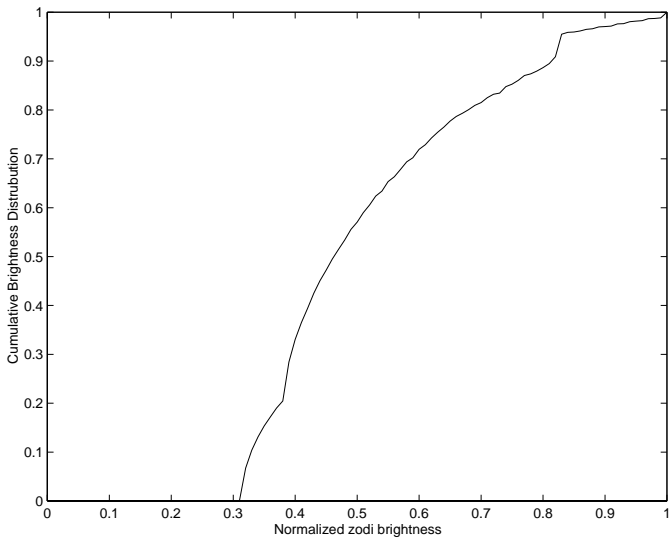
Fig. 8.—Cumulative brightness distribution for the low-energy orbit. The figure presents the percentage of the mission lifetime for which the normalized zodi brightness is below a given value.

Fig. 10.—Time history of the normalized zodi brightness for observation angles of 30°–90° relative to the ecliptic along the high-energy optimal trajectory. Note the dramatic maximum reduction of 97% in brightness. During 82% of the mission lifetime, the zodi brightness is reduced by more than 70%. The spacecraft would observe the sky away from the ecliptic plane; when the spacecraft crossed the ecliptic plane, it would turn over.

Using the methodology proposed by Beichman et al. (1999) for the calculation of mirror diameter, we have found that for the *TPF* IR interferometer, the noise decrease allows a reduction of 20% in mirror diameter, which yields u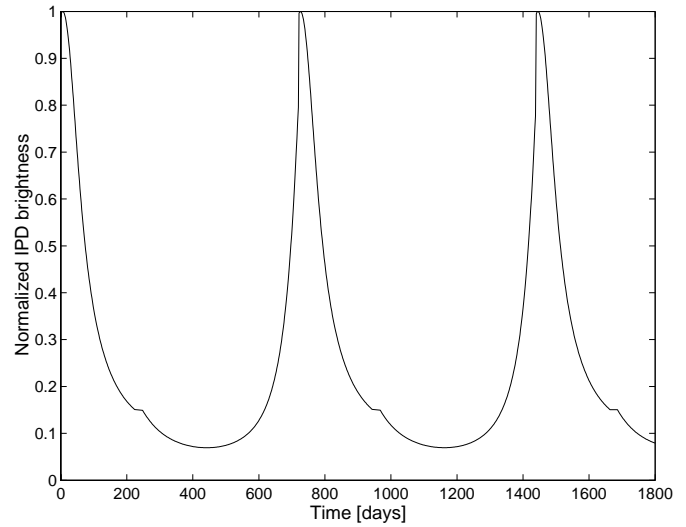p to a 35% reduction in payload mass. This reduction is not included in the optimization. Iteration on the optimization scheme would result in a reduced energy requirement for this reduced mass and perhaps a higher normal displacement.
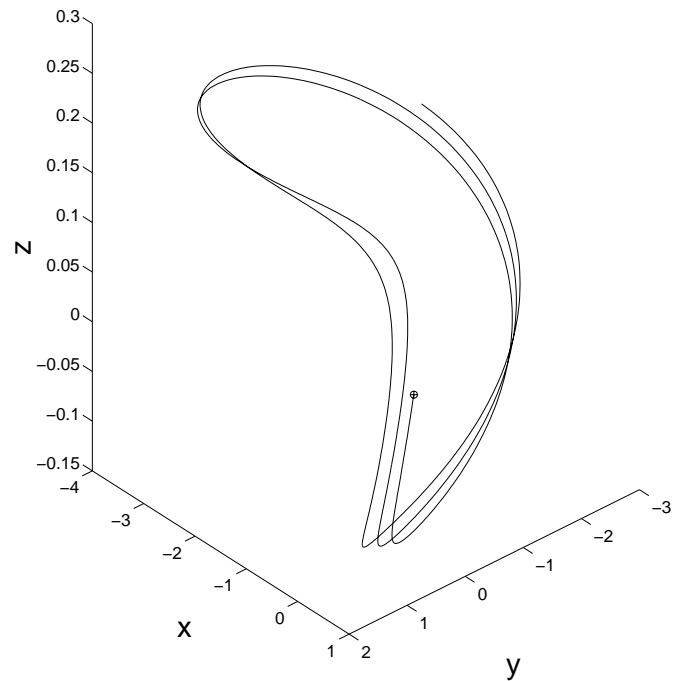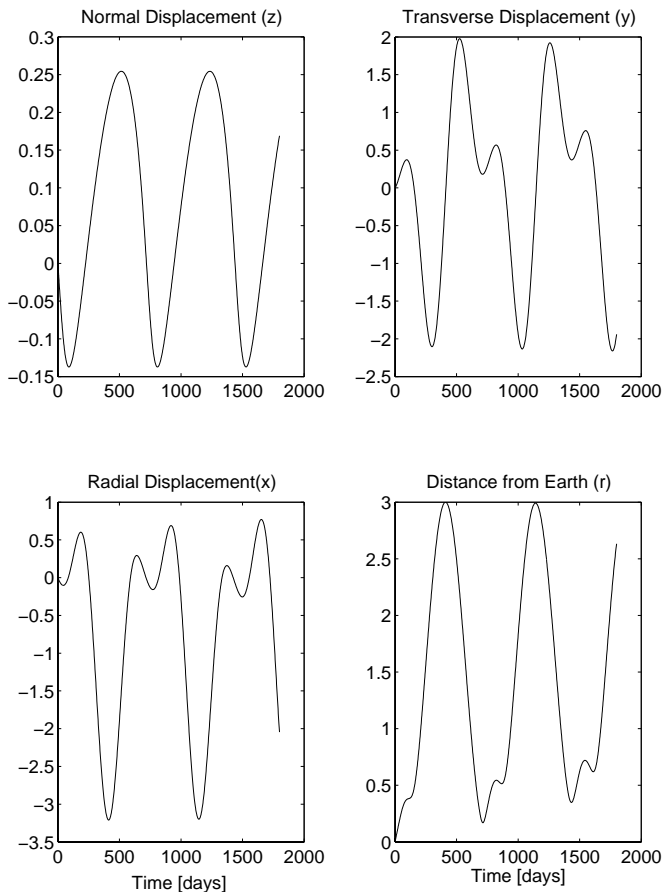

Fig. 9.—Time histories of the displacement components, the three-dimensional trajectory, and the distance from Earth for the high-energy optimal trajectory.
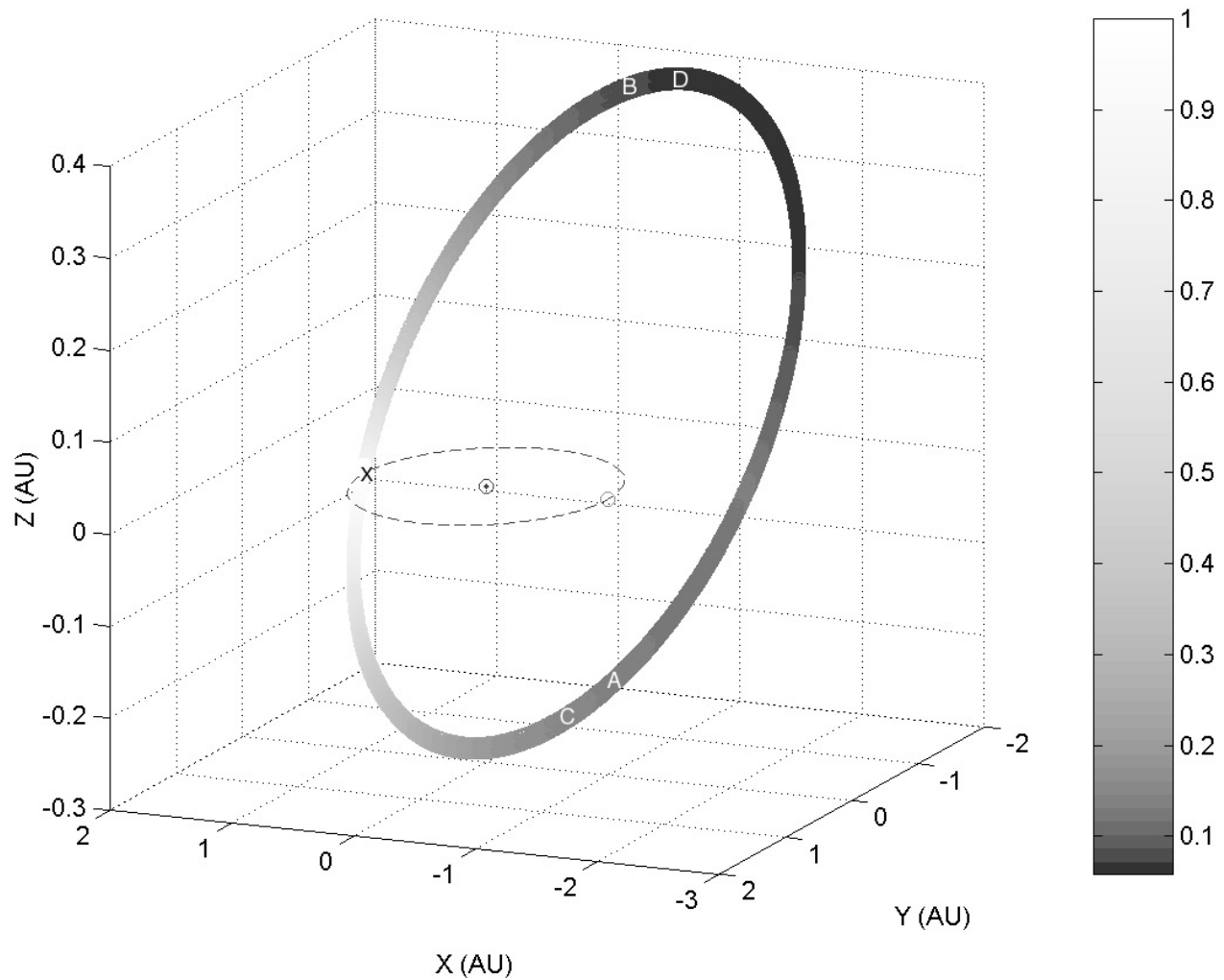
FIG. 11.—Normalized average zodi brightness for the high-energy trajectory, shown in inertial heliocentric-ecliptic coordinates with the position of the Sun indicated by "⊙." A, B, C, and D indicate the position along the trajectory at 6, 12, 18, and 24 months, respectively. The dashed line represents Earth's trajectory, with the position of Earth at 0 and 6 months indicated by the X and O symbols, respectively.
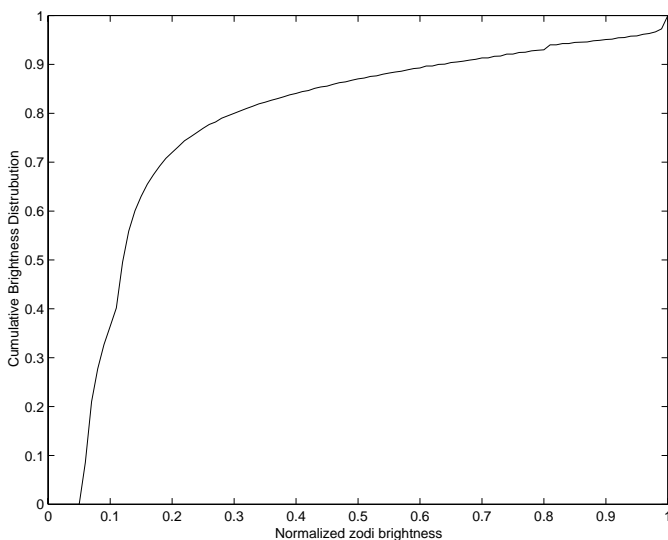

FIG. 12.—Cumulative brightness distribution for the high-energy orbit. The figure presents the percentage of the mission lifetime for which the normalized zodi brightness is below a given value.

3.6. Trajectory Design: High-Energy Optimal Trajectory

The previous section described an optimal trajectory that emerges from a 200 km parking orbit. The constraints $r_{max} \leq 2$ AU and $(v_0)_{max} = 12.7$ km s^{-1} resulted in a type II trajectory that yielded a significant reduction in the zodi brightness. The purpose of this section is to present a different optimal trajectory, which was obtained using other constraints. These constraints represent the maximum lift capability of existing launch vehicles and may even exceed them to some extent. Nevertheless, we have chosen to present this high-energy optimal trajectory because we believe that the energetic requirements for its implementation can be achieved by a future launch vehicle such as the *Evolved Expendable Launch Vehicle* or possibly via a combination of low-thrust electric propulsion and impulsive velocity changes. The principal merit of this trajectory is the outstanding reduction in zodi noise for most of the mission lifetime.

In this new trajectory, we have chosen to start from a 36,000 km geosynchronous orbit, i.e., $(r_0)_{max} = 42,378$ km. Anticipating that the reduction in zodi noise allows the

TABLE 1
PROPERTIES OF THE OPTIMAL TRAJECTORIES

Property	Low-Energy Trajectory	High-Energy Trajectory
Maximum displacement above ecliptic (AU)..........	0.223	0.374
Maximum zodiacal reduction (%)......................	67	97
Fraction of mission/reduction in brightness (%)......	60/50	82/70
Mirror diameter reduction (%)	20	35
Mass reduction (%)	$\lesssim 35$	$\lesssim 50$
Mean distance from Sun (AU).........................	1	1.6
Drift from Earth (AU)	2	3

mass to be reduced by half,[8] we use a 2000 kg payload. With this mass, we choose $C3 = 95$ km^2 s^{-2}, which exceeds—but not by much—the lift capability of the Atlas ARS. This dictates the constraint $(v_0)_{max}$. Also, we let $r_{max} = 3$ AU. Again, the GA optimizer was used to synthesize an optimal trajectory.

Properties of the optimal trajectory are as follows: the trajectory starts from a 36,000 km orbit. The maximum normal deflection above the ecliptic is 0.374 AU with a maximum distance of 3 AU from Earth. As in the previous case, the resulting optimal trajectory drifts away from Earth for a given mission lifetime of 5 yr. It is a non-Keplerian orbit satisfying $0.958 \leq \rho \leq 2.274$. Comparing the frequencies of the in-plane motion with the frequency of the normal motion classifies this trajectory as type III.

Figure 9 shows some of the extraordinary features of the optimal trajectory. This figure depicts the normal, transverse, and radial displacements in the rotating Earth-fixed coordinate system, the three-dimensional trajectory, and the distance from Earth for a 5 yr mission. Note that the minimum approach to Earth is 0.2 AU and is obtained after 802 days (approximately 2.2 yr). The relatively close approach (0.2 AU) means that the orbit might be able to be perturbed to come close enough to Earth for replenishment or maintenance. Thus, this type III trajectory offers somewhat of an advantage over the previously discussed optimal type II trajectory. This specialized feature is typical of type III trajectories.

Similar to the treatment in the previous section, we used the zodi model described in § 2 to estimate the reduction in zodi brightness. Figure 10 describes the normalized zodi brightness as a function of time. The results are dramatic: the maximum reduction in brightness is 97%. Averaging the values over time yields a mean reduction of 75%. During 82% of the mission lifetime, the zodi brightness is reduced by more than 70%. Figure 11 shows a plot of the trajectory in heliocentric coordinates; the intensity of the plot represents the normalized zodi brightness. Note that unlike in Figure 7, the zodi brightness is asymmetric; this is because one of the ecliptic crossings is farther away from the Sun than the other, so the zodi brightness is lower. Figure 12 is the cumulative brightness distribution for this trajectory. This represents the percentage of the mission lifetime for which the normalized zodi brightness is below a certain value. The zodi reduction for this orbit allows for a considerable reduction in telescope mirror size, which not only

results in a remarkable reduction in mass, but moreover, can significantly reduce the development and manufacturing costs.

Using the methodology proposed by Beichman et al. (1999) for the calculation of mirror diameter, we have found that for the *TPF* IR interferometer, the noise reduction due to the high-energy trajectory allows a reduction of 36% in mirror diameter, which yields up to a 50% reduction in payload mass. The properties of the low-energy and high-energy optimal trajectories are summarized in Table 1. This table describes the maximum displacement above the ecliptic, the maximum reduction in zodi brightness, the fraction of mission with the concomitant brightness reduction, the mass reduction, the mean distance from the Sun, and the maximum drift from Earth during the 5 yr mission lifetime.

4. SUMMARY AND DISCUSSION

The zodi is a significant problem for mid-IR missions such as *TPF* because of its strong thermal emission. While this emission can be mitigated by a mission orbit at 5 AU from the Sun (as proposed by Landgraf & Jehn 2001), the associated design aspects render such an orbit infeasible, even though the zodi is considerably reduced. For a finite mission lifetime, the overall scientific return is dramatically reduced because of the time required to get to a 5 AU orbit. Moreover, these trajectories require very large solar arrays and massive communication antennas. Also, in case of a failure, it is practically impossible to replace the damaged components or to perform other replenishment missions. Note also that going a unit distance above the ecliptic decreases the zodi intensity considerably more than going a unit distance from the Sun within the ecliptic. This was the motivation for the study of out-of-the-ecliptic trajectories for space-borne observatories presented in this work. We have used genetic algorithms as the parameter optimization procedure, which has resulted in a fruitful probing of the complex dynamics of the restricted problem. For example, the farthest that either of our design trajectories reaches from the Sun is 2.2 AU within a 5 yr mission lifetime, which means that an order of magnitude smaller solar arrays can be used than for a mission at 5 AU. Also, data collection and scientific interpretation can begin right away, instead of having to wait several years. A direct trip to 5 AU requires a C3 of 80 km^2 s^{-2} (Meissinger, Wertz, & Dawson 1997),[9] equivalent to our high-energy trajectory, and a travel time of 2 yr. Galileo's trajectory used a C3 of 13 km^2 s^{-2} (Meissinger et al. 1997), but it took 6 yr to reach Jupiter, with most of that time spent around 1 AU, and required

---

[8] This is the maximum mass reduction possible for TPF. It is obtained when the zodiacal noise is completely eliminated. Other noise sources, however, prevent further mirror size and mass reduction (Beichman et al. 1999).

[9] Available at http://www.smad.com/analysis/hmeissinger.pdf.

correct planetary alignment to allow for three planetary flybys. Going to 5 AU also means long travel times through the ecliptic plane, which increases the chance of micro-meteorite damage. Finally, we did not iterate on mass reduction in our optimization procedure. The large mass reduction would provide a reduction in launch costs or alternatively an orbit with a greater normal displacement above the ecliptic.

Genetic algorithms have rendered three types of out-of-the-ecliptic trajectories. We believe that the search for trajectory types was thorough within the specified search limits, despite the probabilistic nature of the approach. The trajectory design process used the database of trajectories generated by the characterization process, yet it incorporated tighter parameter constraints. Both the low-energy and the high-energy trajectories obtained by the design process imply that the overall telescope collecting area, and hence the mass and cost, can be significantly reduced. This is due to the substantial reduction in zodi that results from the out-of-the-ecliptic displacement of 0.22 and 0.37 AU for the low- and high-energy trajectories, respectively. For comparison, in typical libration-point trajectories, the normal excursion is up to an order of magnitude smaller. This high displacement also considerably reduces the probability of micrometeorite or space-debris damage, which could extend the mission lifetime.

The mass reduction figures used in this design process are rather specific for a *TPF* mid-IR interferometer looking for terrestrial planets. As the local zodi cloud noise is mitigated, a noise floor is reached. This minimum noise level has specific characteristics derived from the mission itself and is determined by other noise sources that become drivers as we escape the ecliptic. If the trajectories obtained are generalized to other missions, such as filled-aperture telescopes like *NGST* and *SIRTF*, even further benefits in terms of mass reduction are possible. Benefits are not nearly as dramatic for optical missions because the zodi intensity is lower in the visible wavelength region.

The quest for optimal trajectories for space-borne observatories has by no means been exhausted by this study. While the foundation for out-of-the-ecliptic trajectories has been built, there are several additional points that need to be clarified and further investigated. These include optimal transfers from Earth to the initial orbit, use of electric propulsion, searching for optimal initial conditions in other regions of the state space, including perturbations from other solar-system bodies, and using lunar and planetary flybys.

REFERENCES

Beichman, C. A., Woolf, N. J., & Lindensmith, C. A. 1999, The *Terrestrial Planet Finder* (*TPF*) (NASA/JPL 99-3, May 1999; NASA/JPL)
Breakwell, J. V. 1963, in Proc. 14th Int. Astronaut. Congr., Trajectories Launched Normal to the Ecliptic, ed. E. Brun & I. Hersey (Paris: Gauthier-Villars), 128
Buglia, J. J. 1973, J. Spacecr. & Rockets, 10, 601
Gomez, G., Masdemont, J., & Simo, C. 1997, Adv. Astronaut. Sci., 95, 117
———. 1998, J. Astronaut. Sci., 46, 135
Goudas, C. L. 1963, Icarus, 2, 1
Gurfil, P., & Kasdin, J. 2001, J. Astronaut. Sci., in press
Henon, M. 1974, A&A, 30, 317
Howell, K. C., Barden, B. T., & Lo, M. W. 1997, J. Astronaut. Sci., 45, 161
Kelsall, T., et al. 1998, ApJ, 508, 44
Landgraf, M., & Jehn, R. 2001, Ap&SS, 278, 359
Marchal, C. 1990, The Three-Body Problem (New York: Elsevier)
Meissinger, H., Wertz, J., & Dawson, S. 1997, paper presented at the AAS/AIAA Astrodynamics Specialist Conf. (AAS 97-711)
Rabe, E. 1961, AJ, 66, 500
Renard, M. L. 1970, J. Spacecr. & Rockets, 7, 1208
Szebehely, V. 1967, Theory of Orbits (New York: Academic)